PHOTOMASK

BACUS—The international technical group of SPIE dedicated to the advancement of photomask technology.

PUV19 - 3rd Place Zeiss Winner - Best Student Poster

Measuring the Phase of EUV Photomasks

Stuart Sherwin, Laura Waller, and Andrew Neureuther, University of California Berkeley, Department of Electrical Engineering and Computer Science, Berkeley, USA

Isvar Cordova and Patrick Naulleau, Center for X-Ray Optics, Lawrence Berkeley National Laboratory, Berkeley, USA

ABSTRACT

We demonstrate complementary reflectometry and scatterometry methods to measure the phase and amplitude of a patterned EUV photomask at its operating wavelength (13.5nm) and angle range (2 — 10°). We carried out experimental measurements at ALS Reflectometry and Scattering Beamline 6.3.2 on an EUV photomask with a 40-bilayer MoSi multilayer mirror and 60nm TaN absorber. We took three types of measurements: reflectometry for blank multilayer, reflectometry for blank absorber-coated multilayer, and scatterometry for line-space gratings. We used the reflectometry data to fit the Fresnel reflectance amplitude

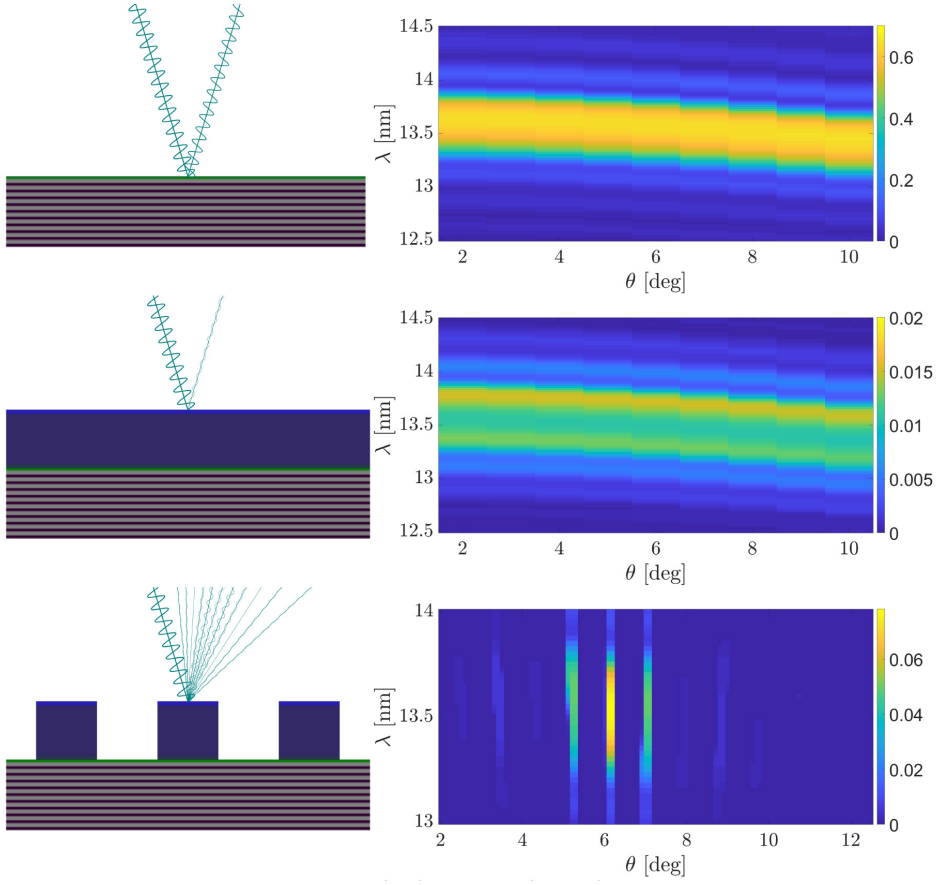

Figure 1. Raw reflectivity data for multilayer (top), absorber (middle), and example scatterometry measurement (bottom).

BACUS NEWS

OCTOBER 2020
VOLUME 36, ISSUE 10

TAKE A LOOK INSIDE:

SPIE.

11147-70

EDITORIAL

The new adolescence of mature photomasks

Thomas Struck, Infineon Technologies

When I grew up in the 1970-ties, it was a given that the younger kids had to wear the clothes and play with the toys of their older brothers and sisters, as the older ones grew out of it. In those times, shirts and pants have been very robust and good enough for more than one generation of kids. Therefore, a lot of kids and teenagers ran around in stylish outdated rags in mint condition. This was not always fun for the younger ones, but it helped a sustainable utilization of goods when budgets were tight.

In the late 1980-ties, I become a mask maker and I learned to adopt a similar business model for photomasks. New equipment was introduced to the marketplace as a key enabler to push the leading-edge capabilities forward, step by step. The engineers fought for every single Nanometer.

Over the years, the tool and the products it makes, becomes mature, on the one hand.

On the other hand, the maturation lowers the cost of a technology node, which leads to an increasing population of products within the node. Engineers drive the capacity gain needed to match the demand, by yield and efficiency improvement on the maturing mask manufacturing tools. After some years, performance of certain tools is getting better compared to the initial acceptance specifications. Lifetime of tools is prolonged again and again by a lot of know-how and efforts in order to keep them alive. At that time, the development of tools moves along with the leading-edge process requirements and leaves the maturing sector behind, unattended.

Now the “old” model does not apply anymore. Especially for a large number of mainstream photomasks, which require slightly more advanced manufacturing technology (e.g. eBeam write-tools), there is no longer enough capacity for mature writing tools and inspection systems for the increasing number of masks needed in mature nodes. Where does this come from? While I’m writing these lines, a robot mower is mowing the lawn, my fridge is telling me that the milk will expire soon and the gear shifter of my bicycle is requesting a firmware update via my smart phone. Thanks to the IoT, AI and an increasing amount of gadgets, which can get manufactured in a cost effective manner on mature nodes, the demand for mainstream masks is increasing a lot. This trend will continue. As a consequence, the supply of mature photomasks getting tighter.

How to overcome this situation? There are a bunch of ongoing activities to try, as much as possible, and keep the existing systems up and running, with all the difficulties caused by the missing spare parts, obsolescence of electronics and service. But meanwhile, there is also a business case to develop new tools to tackle the existing mature mask market. Those tools are optimized to achieve maximum throughput. Thereby, a new challenge arises: New tools always depreciate which raises the BOM cost for each product made. This increase in the cost does not help the competitiveness of these types of products which are already on a fierce cost down roadmap. Therefore the story continues: Engineers have to fight. This time they have to fight for every single $.

BACUS

N • E • W • S

BACUS News is published monthly by SPIE for *BACUS*, the international technical group of SPIE dedicated to the advancement of photomask technology.

Managing Editor/Graphics Linda DeLano

SPIE Sales Representative, Exhibitions, and Sponsorships Melissa Valum

BACUS Technical Group Manager Marilyn Gorsuch

SPIE.

P.O. Box 10, Bellingham, WA 98227-0010 USA
Tel: +1 360 676 3290
Fax: +1 360 647 1445
SPIE.org
help@spie.org

Shared Layers	Absorber Layers
Thickness [nm] Ru	Thickness [nm] TaON
Thickness [nm] Ru2Si3	Thickness [nm] TaN
Thickness [nm] Si	Thickness [nm] TaNRu
Thickness [nm] MoSi2	RMS Roughness [nm] TaON
Thickness [nm] Mo	RMS Roughness [nm] TaN
Thickness [nm] MoSi2	RMS Roughness [nm] TaNRu
RMS Roughness [nm] Ru	Composition [%] TaON - Ta
RMS Roughness [nm] Ru2Si3	Composition [%] TaON - N
RMS Roughness [nm] Si	Composition [%] TaON - O
RMS Roughness [nm] MoSi2	Composition [%] TaN - Ta
RMS Roughness [nm] Mo	Composition [%] TaN - N
Composition [%] Ru - Ru	Composition [%] TaNRu - Ru
Composition [%] Ru2Si3 - Ru	Composition [%] TaNRu - Ta
Composition [%] Ru2Si3 - Si	Composition [%] TaNRu - N
Composition [%] Si - Si	
Composition [%] MoSi2 - Si	
Composition [%] MoSi2 - Mo	
Composition [%] Mo - Mo	Etch Layers
Composition [%] MoSi2 - Si	Thickness post-etch [nm]
Composition [%] MoSi2 - Mo	RMS Roughness post-etch [nm]

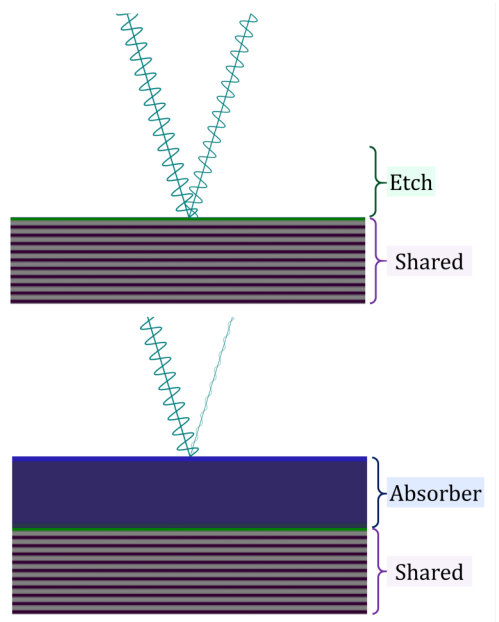

Figure 2. Film-stack model parameters. Each layer has a thickness, RMS surface roughness, and a composition of each atomic species.

by adjusting the thickness, atomic density, and interface roughness of multilayer and absorber layers. We then fit the scatterometry data using a thin-mask approximation. The advantage of reflectometry is the higher level of model fidelity (2 — 4% vs 6% — 15% error), whereas the advantage of scatterometry is its direct sensitivity to relative phase through spatial interference. Despite differences between the two approaches, both gave similar phase values, mutually-consistent to within $\pi/51$ RMS. We observe the phase to vary from $0{:}78\pi$ at 2° to $0{:}88\pi$ at 10°, suggesting that engineering phase effects to improve image contrast will need to consider phase values across a range of illumination angles rather than simply the chief ray.

Introduction

The pattern on an EUV photomask is comprised of two regions: absorber and multilayer. The Fresnel reflection coefficients from these two regions, together with a binary mask layout, give an approximate thin-mask estimate for the near-field reflection function, which is the contribution of the photomask to forming the aerial image. The relative phase of these two reflection coefficients determines whether they will interfere constructively or destructively; the relative amplitude determines the magnitude of this interference. In this work, we attempt to measure this relative phase and amplitude using reflectometry and scatterometry.

Section 1 details the measurements taken, which include reflectivity vs wavelength and angle for multilayer and absorber, as well as diffraction efficiency vs wavelength and angle for 8 line-space gratings. Section 2 outlines how we parametrize the EUV photomask. Section 3 describes how we fit the model to our measured data. Section 4 discusses theoretical guarantees of causality and phase uniqueness, and to what extent they can be leveraged for this problem. Section 5 presents the recovered phase and amplitude from each modality and provides some interpretation of the results.

1. Measurements

We conducted reflectivity measurements on an EUV photomask with a 40-bilayer MoSi multilayer mirror and 60nm TaN absorber at the Advanced Light Source (ALS) Beamline 6.3.2, summarized in Fig. 1. We acquired reflectometry measurements on the absorber and multilayer regions, as well as scatterometry measurements on 8 line-space gratings. Gratings have pitch (p) ranging from roughly 300-1300nm (75-325nm at wafer scale), and nominal duty cycle (D) either 1/2, 1/3, or 1/4.

Reflectometry measurements consist of 101 wavelengths (λ) from 12.5-14.5nm and 9 angles (θ) from 2-10°, for a total of 909 measurements of absorber and multilayer (1818 total). Fig. 1 (top) shows the multilayer reflectivity as a function of wavelength and angle. The reflectivity at nominal operating conditions is $R(\theta = 6°, \lambda = 13.5\text{nm}) = 62.8\%$, which is close to the maximum reflectivity of $R(\theta = 10°, \lambda = 13.46\text{nm}) = 64.7\%$. However, Fig. 1 (middle) tells a more surprising story about the absorber-coated multilayer: now at 6°, 13.5nm there is a local minimum in reflectivity of 1.1%, suggesting interference between multiple reflections. Notably, the combination of high multilayer reflectivity and low absorber reflectivity is ideal for achieving amplitude-based contrast.

Scatterometry measurements consist of 41 wavelengths from 13-14nm, 4 illumination angles at 2-8°, and 106 detector angles from 2-12.5°. Raw data for one illumination angle is shown in Fig. 1 for illustration. We determine the exact pitch and angle of illumination from the angles of diffraction orders, then extract diffraction efficiencies with a local maximum. In our analysis we considered 5 diffraction efficiencies (-2:2) per illumination condition, provided the diffraction order fell within the measured range of angles, or around 700 diffraction efficiencies per grating. Note that the exact number of measured diffraction efficiencies varies for each grating: negative orders can diffract to angles smaller than 2°, while positive orders can diffract to angles larger than 12.5°. Because gratings with smaller pitch diffract light to larger angles, smaller features tend to have fewer measured diffraction orders.

2. Model

We consider a binary mask, with discrete regions of absorber and multilayer. We employ a thin-mask stack-Kirchhoff model where the electric near-field is approximated as:

$$E(x, y\,; \lambda, \theta) = r_{Abs}(\lambda, \theta) + [r_{ML}(\lambda, \theta) - r_{Abs}(\lambda, \theta)]\, p(x, y), \quad (1)$$

where p is the mask layout, E is the near-field, and r_{Abs} and r_{ML} are the Fresnel reflection coefficients of the absorber and multilayer, respectively. For a 1D grating pattern, we can further simplify the equation. We model

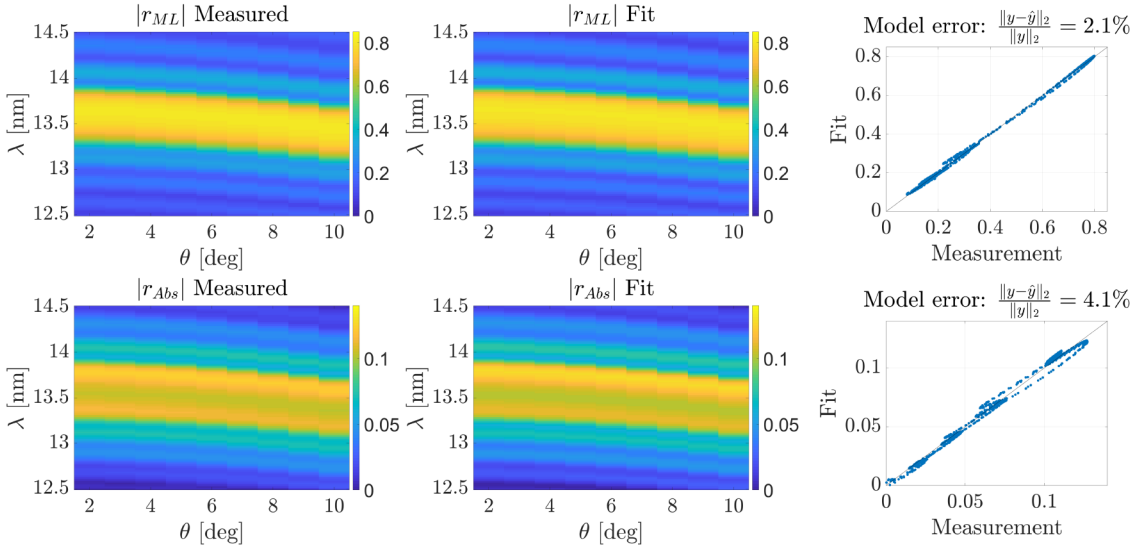

Figure 3. Reflectometry fit for multilayer (top) and absorber (bottom). Left to right: measured amplitude, fitted amplitude, correlation.

our pattern as a square-wave of pitch p and duty cycle D. From Fourier diffraction theory[1] we find the diffraction efficiencies (s_j, $j = -N, \ldots, N$) to be:

$$s_j = \begin{cases} r_{Abs} + (r_{ML} - r_{Abs})\, D, & j = 0 \\ (r_{ML} - r_{Abs})\, \frac{\sin(\pi j D)}{\pi j}, & j \neq 0 \end{cases} \quad (2)$$

We calculate Fresnel coefficients via the Transfer-Matrix Method, which accounts for all infinite reflections by solving Maxwell's equations exactly in 1D,[2] and depends on layer thickness, index of refraction, and surface roughness.[3] Index of refraction is calculated[4] from atomic density and atomic scattering factors tabulated in the CXRO database.[5] If a layer contains m atomic species, it will have $2+m$ parameters: thickness, roughness, and density of each atomic species. The multilayer consists of 2 capping layers (Ru, Ru2Si3) and 4 periodic layers (Si, MoSi2, Mo, MoSi2) repeated 40 times. The absorber consists of a primary TaN layer as well as a TaON anti-reflection coating and a TaRuN interdiffusion layer with the Ru multilayer cap. The etched region is allowed to have 1 additional layer (TaRuN), which is meant to represent "scum" or incomplete etching of absorber; in practice this layer was found to have approximately 0 thickness, but nonzero roughness (0:4nm RMS), suggesting a complete etch leaving behind a slightly rough surface. MoSi2 interdiffusion thickness, as reported in the literature,[6] was fixed to be approximately 0.6nm for Mo-on-Si and 0.95nm for Si-on-Mo.

We assume a linear model for calculating complex refractive index ($n = 1 - \delta - i\beta$), which assumes that δ and β are linear with the density of each atomic species. This assumption of linearity becomes increasingly more accurate for $\delta, \beta \ll 1$, which occurs in the limit of high photon energies, but is nonetheless a reasonable approximation in the EUV regime.[4] So for the index of refraction calculation we take a weighted sum of δ and β for each constituent material at nominal material density.[7] Particularly, say we have a set of materials, M. If layer k is composed of elements $\varepsilon_k \subseteq M$, then the refractive index is:

$$n_k = 1 - \sum_{j \in \varepsilon_k} w_{jk} \left(\delta_0^j + i\beta_0^j \right), \quad (3)$$

where w_{jk} is the weighting factor for element j in layer k, and δ_0^j, β_0^j are the nominal δ and β for element j. We refer to each weighting factor as the "composition" of a particular element. Note that we do not constrain the total composition to sum to 1, allowing the model to account for changes in material density.

In addition to thickness and composition, there could also be interfacial roughness between any two layers. We treat this roughness as a correction to the reflection and transmission coefficients of each interface in the transfer-matrix calculation, which removes energy and induces a phase shift. These corrections represent interference of reflections or transmissions from an ensemble of interfaces with a Gaussian surface-height distribution; the statistical effects of this Gaussian are characterized by its standard deviation, i.e. the RMS roughness at the interface.[3]

In total there are 36 parameters, summarized in Fig. 2 and listed in Table 1. The number of parameters can likely be reduced further in a manufacturing setting where more is known *a priori*. However, we feel that our set of parameters reflects realistic uncertainties in a research environment: we do not know exactly the density with which films are deposited, the roughness of interfaces, or the thickness of each layer. We do however assume exact prior knowledge of atomic scattering factors,[5] and approximate prior knowledge of layer thicknesses and elemental composition.

3. Fitting

We fit both reflectometry and scatterometry data according to the model described in Section 2. Particularly, we use the Fresnel reflection coefficient amplitude of the absorber and multilayer for reflectometry, and the Fresnel thin-mask diffraction amplitude for scatterometry (Eqn. 2). We carry out the fitting sequentially: first reflectometry, followed by scatterometry. In reflectometry, we fit on reflectivity measurements from both absorber and multilayer simultaneously to find the parameters shown in Fig. 2. In scatterometry, we initialize with the fitted film-stack from reflectometry and the nominal value for D (duty-cycle) and update D as well as 6 parameters describing absorber layers (listed in Table 2).

The fitting framework for both reflectometry and scatterometry is nonlinear least-squares. For either case assume we have m amplitude measurements and d parameters. We define the measured data as $\mathbf{y} \in \mathbb{R}^m$, the forward model as $\mathbf{f} : \mathbb{R}^d \to \mathbb{R}^m$, and the model parameters as $\mathbf{x} \in \mathbb{R}^d$ (reflectometry: $m = 1818$; $d = 36$; scatterometry: $m \approx 700$; $d = 7$). The forward model $\mathbf{f}$ captures the reflected or scattered amplitude for each incident wavelength and angle, and $\mathbf{x}$ contains the physical parameters listed in Tables 1 and 2. To account for scattering background and unknown systematic errors, errors we also apply a scaling and offset determined by projecting the measured data onto the range of the matrix $\mathbf{A}(\mathbf{x}) = [1\ f(x)]$. Least-squares projection is computed via the matrix pseudo-inverse (denoted †) as $\hat{\mathbf{y}}(\mathbf{x}, \mathbf{y}) = \mathbf{A}(\mathbf{x})\mathbf{A}^\dagger(\mathbf{x})\mathbf{y}$. Therefore we define our loss function

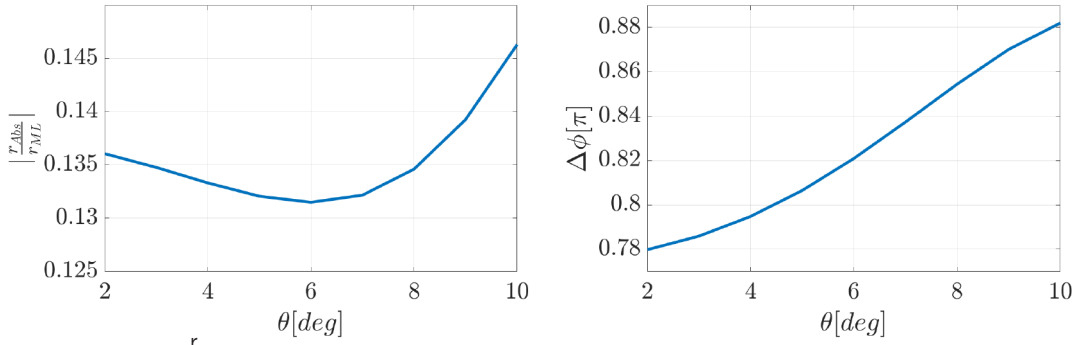

Figure 4. Amplitude and phase of $\frac{r_{Abs}}{r_{ML}}$ vs illumination angle at λ = 13:5nm, as determined by reflectometry.

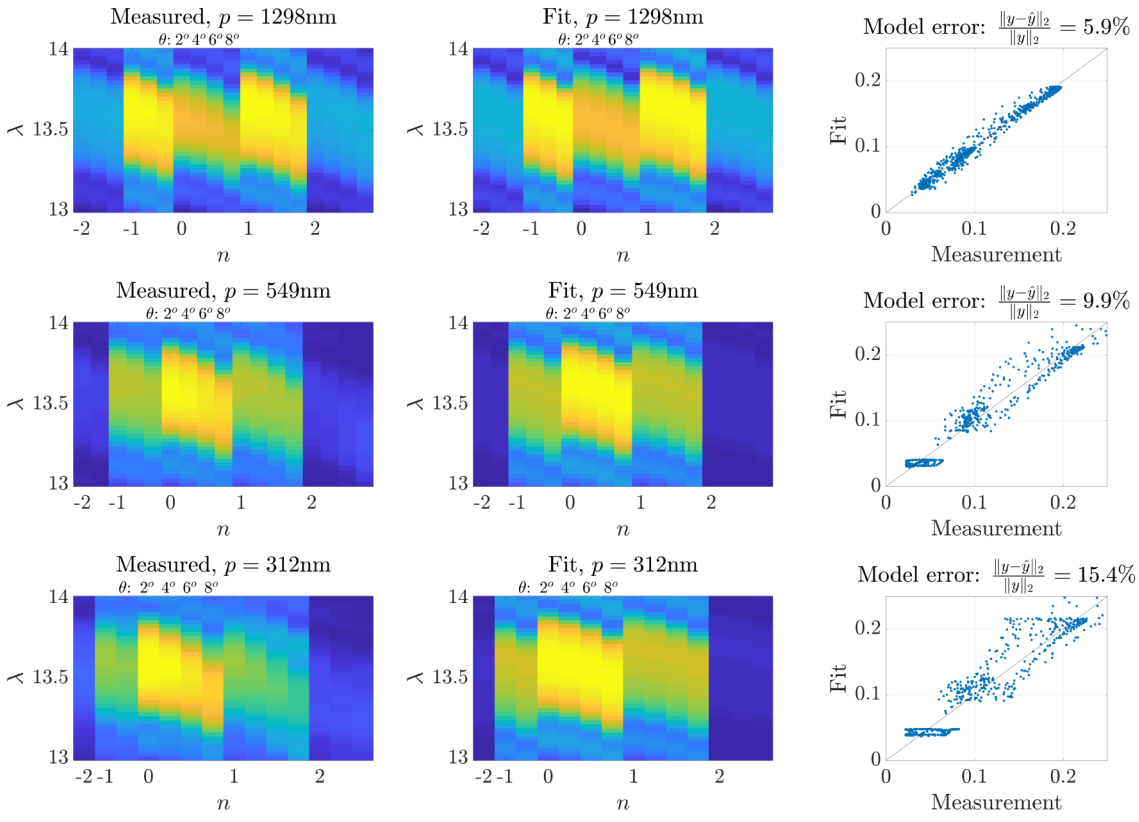

Figure 5. Scatterometry fit for p = 1298nm (top), p = 549nm (middle), and p = 312nm (bottom). Left to right: measured amplitude, fitted amplitude, correlation.

as $\mathcal{L}(\mathbf{x}) = \|\mathbf{y} - \mathbf{A}(\mathbf{x})\mathbf{A}(\mathbf{x})^{\dagger}\,\mathbf{y}\|_2^2 = \|\mathbf{y} - \hat{\mathbf{y}}(\mathbf{x}, \mathbf{y})\|_2^2$.

This projection is simply a redefinition of the least-squares loss function in terms of correlation rather than direct subtraction. We take this approach because our problem is highly sensitive to systematic error, and even a small amount of calibration error or model mismatch could dominate the loss function. Although we do already take efforts to account for possible systematic effects, to safely neglect systematic error we need it to be much smaller than the residual error, which is 2 – 4% for reflectometry. This amounts to requiring the systematic error to be multiple orders of magnitude lower than the signal. The potential downside of projecting onto the range of **A** is that it effectively reduces the dimension of our output space by rank [**A**] = 2. In our case, because the number of measurements is much greater than 2, this effect is quite small. Therefore, we believe that in this case the drawbacks of slightly reducing the dimension of the output space are overwhelmed by the benefits of mitigating small additive or multiplicative systematic errors.

To leverage our approximate *a priori* knowledge of the parameters, we restrict our solution to some feasible set $S \subseteq \mathbb{R}d$, which in our case includes upper and lower bounds for every variable (summarized in Tables 1 and 2). Thus our optimization problem becomes:

$$\min_{x \in S} \left\| y - \hat{y}(x, y) \right\|_2^2 \qquad (4)$$

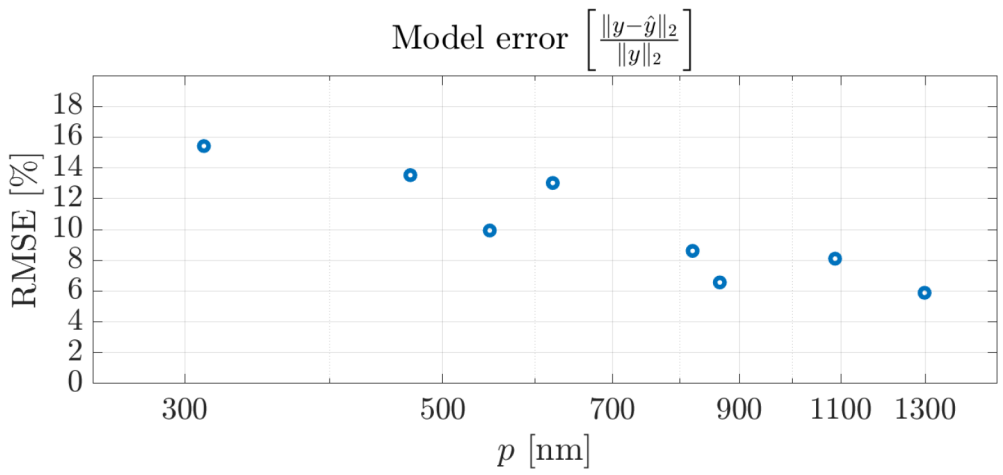

Figure 6. Scatterometry error vs pitch; the clear trend of worse error for smaller pitch suggests substantial mask 3D effects are impacting the performance of the thin-mask model.

However, this nonlinear least-squares loss function is non-convex, meaning that common solvers such as gradient descent will be prone to converge to erroneous local minima rather than the true global minimum. As such, we employ a non-convex approach to solve this minimization. At a high level, we attempt to find the global minimum by: (1) exploring the parameter space near the current solution; (2) identifying promising directions; and (3) performing line searches in these directions. This procedure is repeated for a *M* iterations. On each iteration, we:

1. Locally explore the space by evaluating a set of n random perturbations of the current solution: $x_j = x + \Delta_j$, $\Delta_j \overset{iid}{\sim} N(0, \sigma)$, $j = 1, ..., n$. For each of these perturbations, if $\mathcal{L}(x_j) < \mathcal{L}(x)$, we update $x \rightarrow x_j$.
2. Identify promising directions by sorting x_j from lowest to highest MSE, and putting the first n_1 perturbations into a matrix $Y = [\, f(x_1) \ldots f(x_{n_1}) \,]$. We compute the k-SVD $Y \approx U_k S_k V_k^H$ to obtain a reduced set of k coordinates $B = U_k^H Y \in \mathbb{R}^{k \times n_1}$. Then for each row of B ($i = 1, ..., k$), we identify columns containing the minimum and maximum values ($n_{max,i}$ and $n_{min,i}$). We define our search direction as $a_i = x_{nmax,i} - x_{nmin,i}$, which represents the difference in parameters between two extreme points in dimension i selected from among the n1 best perturbations.
3. For each row of B, $i = 1, ..., k$, perform a line-search sampling m points centered about the current solution in the direction a_i, updating our solution if a lower MSE is achieved.

For our work, we used $M = 50$ iterations, $n = 100$ random perturbations, $k = 5$ SVD dimensions, and $m = 100$ points per line search, for a total of $M(n + km) = 30{,}000$ function evaluations to find a solution.

This approach is less computationally efficient than a gradient-based solver (50 iterations x 36-point finite difference stencil = 1800 function evaluations), but generally converges to a more accurate solution. In any event, due to the computational efficiency of our model in this work, the number of function evaluations is not of great practical concern. However, the relatively large number of function evaluations does impose practical limitations on the type of model we can employ. Particularly, in scatterometry we know that 3D effects will impact the accuracy of the thin-mask model, especially as the pitch decreases.[8-11] One approach to overcome this issue would be to explicitly model all 3D effects using Rigorous Coupled-Wave Analysis (RCWA). However, we found that this would lead to an unacceptable increase in the runtime; from 30k evaluations in 204s for our method to a single evaluation in 186s for RCWA (same 164 illumination conditions). To fit a single scatterometry grating at this rate (single-threaded) would take 64 days as opposed to just over 3 minutes.

In addition to runtime, other practical concerns are that it is unclear how to include random surface roughness or how to sufficiently parametrize the 3D structure. That said, integrating RCWA into the scatterometry analysis may be beneficial and should be a subject of future work.

4. Uniqueness

When solving a non-convex problem such as this, an important question of the uniqueness of the solution arises. On the one hand, if our *a priori* knowledge of the system were sufficiently accurate, the solution to Eq. 4 could be made unique by sufficiently restricting the range of feasible parameters. On the other hand, this approach would require such a degree of prior knowledge as to beg the question of why to perform the measurement in the first place. As such, in our analysis we try to make as few restrictive assumptions as possible. Instead, we hope to rely on having many more measurements than model parameters, making justified physical assumptions, and benefiting from physical insights about the nature of causal functions.

For any causal function, the amplitude and phase are linked. Furthermore, any Fresnel reflection coefficient is a causal function. Therefore, as we measure the amplitude of the Fresnel reflection coefficient over a range of wavelengths, we also implicitly gain information about its phase. Mathematically, this is described by the Kramer's-Kronig (KK) relations, which imply that the phase can be directly computed by a locally-weighted integral of the log-amplitude over all frequencies (photon energies):

$$\phi(\omega) = \frac{1}{\pi} P \int_0^\infty \frac{\log |r(\omega')|}{\omega' - \omega} d\omega' \tag{5}$$

Therefore, if we have any causal function whose amplitude matches $|r(\omega)|$ for all frequencies ω, then it must also have the correct phase (up to a global offset). If instead we have a function that matches $|r(\omega)|$ for only a finite range of frequencies, we can make a looser statement that the phase error is bounded (again up to an offset). A similar statement can be made for a function that does not match the measured data exactly, but does approximately over some finite range.[12] Concretely, let the true coefficient be $r_{true} = |r_{true}| e^{i\phi_{true}}$. Define $\delta\phi = \phi - \phi_{true}$, $\delta \log |r| = \log |r(\omega')| - \log |r_{true}(\omega')|$, and the measurement range to be $[a, b]$. Then we can write:

$$\delta\phi(\omega) = \frac{1}{\pi} P \int_0^\infty \frac{\delta \log |r|}{\omega' - \omega} d\omega' \tag{6}$$

$$\delta\phi(\omega) = \frac{1}{\pi} P \int_0^\infty \frac{\delta \log |r|}{\omega' - \omega} d\omega' = \frac{1}{\pi} P \int_0^a \frac{\delta \log |r|}{\omega' - \omega} d\omega' + \frac{1}{\pi} P \int_a^b \frac{\delta \log |r|}{\omega' - \omega} d\omega' + \frac{1}{\pi} P \int_b^\infty \frac{\delta \log |r|}{\omega' - \omega} d\omega' \tag{7}$$

$$= \varepsilon_{[0,a]} + \varepsilon_{[a,b]} + \varepsilon_{[b,\infty)}, \tag{8}$$

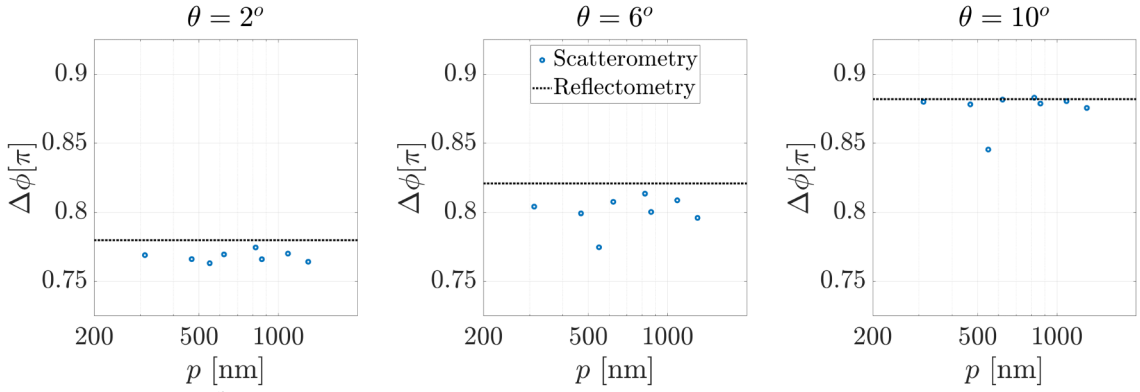

Figure 7. Amplitude and phase of $\frac{r_{Abs}}{r_{ML}}$ vs pitch at λ = 13:5nm and θ = 2; 6; 10° [left to right], as determined by scatterometry. Reflectometry result is shown in black dotted line for reference.

where we have defined the error terms $\varepsilon_{[c,d]} = \frac{1}{\pi} P \int_c^d \frac{\delta \log|r|}{\omega' - \omega} d\omega'$.

These three terms can be interpreted as: $\varepsilon_{[0,a]}$, the error in the extrapolation to low frequencies; $\varepsilon_{[a,b]}$, the error in the measured frequency range; and $\varepsilon_{[b,\infty)}$, the error in the extrapolation to high frequencies. So the error in the phase can stem from model error ($\varepsilon_{[a,b]}$), which is directly minimized by our optimization procedure; or extrapolation error ($\varepsilon_{[0,a]}$, $\varepsilon_{[b,\infty]}$), which diminishes in importance further from the measured range, and should be much better than the worst-case since we have known atomic scattering factors and approximately known geometries. Therefore, simply by finding any Fresnel coefficient approximately matching the measured amplitude over a sufficiently long range of data, we can have some confidence that the phase is at least approximately correct.

However, there is one additional source of phase error that cannot be addressed by a causality argument: a constant phase offset for all frequencies. The phase offset of a single coefficient is physically insignificant, but since both r_{Abs} and r_{ML} could have different offsets, a constant error in the relative phase could arise. To be clear: the relative phase can be predicted by our model, but it relies on the assumption of a common reference plane of the multilayer top surface. If we were unfortunate enough to find a model with the same amplitude for both coefficients but a relative phase shift, it would be indistinguishable from the true model. Such a solution may not exist, indeed likely does not exist within our feasible set *S*, but the fact that it could exist implies that reflectometry can never be directly sensitive to relative phase, only indirectly through a model.

So, while these causality-based guarantees heavily constrain the solution, unfortunately they fall just short of making the case that reflectometry can unambiguously measure the relative phase. This is where scatterometry becomes an invaluable supplement to reflectometry: it is directly sensitive to relative phase of r_{Abs} and r_{ML}, Δφ. Taking the amplitude-squared of Eq. 2:

$$|s_j|^2 = \begin{cases} |r_{Abs}|^2(1-D)^2 + |r_{ML}|^2 D^2 + 2|r_{Abs}||r_{ML}|(1-D)D\cos(\Delta\phi), & j = 0 \\ \left[|r_{Abs}|^2 + |r_{ML}|^2 - 2|r_{Abs}||r_{ML}|\cos(\Delta\phi)\right]\left(\frac{\sin(\pi j/D)}{\pi j}\right)^2, & j \neq 0 \end{cases} \quad (9)$$

In particular, note the emergence of cos (Δφ) terms. Repeating the same thought experiment from reflectometry, if we had a model with the same amplitude for both coefficients but a relative phase shift, in this case we would observe a change in the measured signal.

5. Results

Fig. 3 shows the measured and fitted Fresnel coefficient amplitude for multilayer and absorber. We obtain relative RMS error ($\frac{\|y-\hat{y}\|_2}{\|y\|_2}$) of 2% for multilayer and 4% for absorber. From the causality argument presented in Section 4, this implies that the phase of absorber and multilayer are likely accurate, possibly up to some constant offset. We plot the ratio ($r_{Abs}\, r_{ML}$) as a function of angle at λ = 13:5nm in Fig. 4, which shows that the phase varies almost linearly across the illumination pupil from 0:78π at 2° to 0:88π at 10°. This suggests that engineering phase effects to improve image contrast will need to account for phase across a range of illumination angles rather than just the chief ray. Effectively, this represents a type of "thin-mask 3D effect", where angular variation in the near-field arises from thin-film interference purely in the *z* direction; this can be distinguished from mask 3D effects such as shadowing, which involve interactions between lateral and axial dimensions.

Fig. 5 shows three representative measurements for the largest and smallest features, plus one intermediate pitch. Note that agreement is much better for the larger pitch (*p* = 1298nm), somewhat degraded for the middle pitch (*p* = 549nm), and even further degraded for the smaller pitch (*p* = 312nm), although there is still qualitative agreement in all cases. Shadowing effects can be directly observed by comparing the measured (left) and fitted (right) diffraction efficiencies. Shadowing is strongest for larger angles and smaller features,[8-11] and generally reduces the amplitude of the image. Particularly, it reduces the average, or 0 order amplitude. We observe this clearly in the drop of 0 order amplitude at 8° compared to lower angles. The drop is by far the strongest for *p* = 312nm, is still observable but less prominent for *p* = 549nm, and is barely perceptible for *p* = 1298nm. On the other hand, the same darkening is not apparent in the any of the fitted models because the thin-mask model neglects shadowing. Fig. 6 explicitly shows the (expected) trend of lower error for larger features. Therefore, to use this approach it is recommended to measure larger pitches, in this analysis *p* ≥ 800nm. Modeling smaller features with greater fidelity could be resolved by using a more rigorous solver; but, as mentioned, it would take orders of magnitude longer to use RCWA, in addition to further complications discussed in Sec. 3.

Fig. 7 plots the agreement between reflectometry and scatterometry at three angles (2°; 6°; 10°). Qualitatively, it is apparent that except for one outlier at *p* = 549nm, all features show very similar phase values. Quantifying the self-consistency, we find that the phase values recovered from scatterometry are mutually consistent to within π=88 (1σ), and are consistent with the phase values from reflectometry to within π=51 (RMS). Note that all recovered phase values show the same trend vs angle, with a deviation of roughly $\frac{\pi}{10}$ as the angle varies from 2°—10°. This implies that the phase cannot be assumed constant vs angle, and that EUV phase-shift masks should be designed considering a range of illumination angles and not only the chief ray.

Conclusion

We have demonstrated measurement of the phase and amplitude of an EUV photomask with a 40-bilayer MoSi multilayer mirror and 60nm TaN absorber. We determined the phase to vary almost linearly from 0:78π at 2° to 0:88π at 10°, suggesting that optimally leveraging phase effects to improve image contrast will need to account for phase across a range of illumination angles rather than just the chief ray. Scatterometry for different features was consistent to within π/88 1σ, while reflectometry and scatterometry were consistent with each other to within π/51 RMS. Scatterometry data clearly shows a trend of higher error for smaller pitches, suggestive of substantial mask 3D effects; these effects are largely mitigated by measuring gratings with p > 800nm. In the future we also plan to validate these results against an alternative approach of actinic quantitative phase-imaging.

Acknowledgments

This research is sponsored by C-DEN (Center for Design-Enable Nanofabrication). Member companies — ARM, ASML, Cadence, Carl Zeiss Group, Intel, KLA-Tencor, Mentor Graphics, and Qualcomm.

This work was performed in part at Lawrence Berkeley National Laboratory which is operated under the auspices of the Director, Office of Science, of the U.S. Department of Energy under Contract No. DE-AC02-05CH11231.

References

[1] C. Mack, *Fundamental principles of optical lithography: the science of microfabrication*, John Wiley & Sons, 2008.

[2] J. W. Goodman, *Introduction to Fourier optics*, Roberts and Company Publishers, 2005.

[3] C. C. Katsidis and D. I. Siapkas, "General transfer-matrix method for optical multilayer systems with coherent, partially coherent, and incoherent interference," **Applied optics 41**(19), pp. 3978-3987, 2002.

[4] D. Attwood and A. Sakdinawat, *X-rays and extreme ultraviolet radiation: principles and applications*, Cambridge university press, 2017.

[5] B. L. Henke, E. M. Gullikson, and J. C. Davis, "X-ray interactions: photoabsorption, scattering, transmission, and reflection at e= 50-30,000 ev, z= 1-92," *Atomic data and nuclear data tables* **54**(2), pp. 181-342, 1993.

[6] A. Aquila, F. Salmassi, F. Dollar, Y. Liu, and E. Gullikson, "Developments in realistic design for aperiodic mo/si multilayer mirrors," *Optics express* **14**(21), pp. 10073-10078, 2006.

[7] *Periodic Table of the Elements*, (accessed August 26, 2019). Available at https://www.csun.edu/science/ref/spreadsheets/xls/elements.xls.

[8] H. Song, L. Zavyalova, I. Su, J. Shiely, and T. Schmoeller, "Shadowing effect modeling and compensation for euv lithography," in *Extreme Ultraviolet (EUV) Lithography II*, **7969**, p. 79691O, International Society for Optics and Photonics, 2011.

[9] H. Kang, S. Hansen, J. van Schoot, and K. van Ingen Schenau, "Euv simulation extension study for mask shadowing effect and its correction," in *Emerging Lithographic Technologies XII*, **6921**, p. 69213I, International Society for Optics and Photonics, 2008.

[10] S. Sherwin, L. Waller, A. Neureuther, and P. Naulleau, "Advanced multilayer mirror design to mitigate euv shadowing," in *Extreme Ultraviolet (EUV) Lithography X*, **10957**, p. 1095715, International Society for Optics and Photonics, 2019.

[11] S. Sherwin, A. Neureuther, and P. Naulleau, "Actinic euv scatterometry for parametric mask quantification," in *Extreme Ultraviolet (EUV) Lithography IX*, **10583**, p. 105831G, International Society for Optics and Photonics, 2018.

[12] R. Ahrenkiel, "Modified kramers—kronig analysis of optical spectra," *JOSA* **61**(12), pp. 1651-1655, 1971.

Table 1. Reflectometry model parameters.

	Min	Fit	Max
Thickness [nm] TaON	1.980	2.019	2.020
Thickness [nm] TaN	57.420	58.132	58.580
Thickness [nm] TaNRu	0.490	0.501	0.510
Thickness [nm] Ru	1.980	2.019	2.020
Thickness [nm] Ru2Si3	0.990	0.996	1.010
Thickness [nm] Si	3.208	3.264	3.272
Thickness [nm] MoSi2	0.590	0.602	0.610
Thickness [nm] Mo	2.138	2.151	2.182
Thickness [nm] MoSi2	0.940	0.959	0.960
RMS Roughness [nm] TaON	0.000	0.023	0.100
RMS Roughness [nm] TaN	0.000	0.129	1.000
RMS Roughness [nm] TaNRu	0.000	0.006	0.100
RMS Roughness [nm] Ru	0.000	0.010	0.100
RMS Roughness [nm] Ru2Si3	0.000	0.051	0.100
RMS Roughness [nm] Si	0.000	0.099	0.100
RMS Roughness [nm] MoSi2	0.000	0.014	0.100
RMS Roughness [nm] Mo	0.000	0.040	0.100
Composition [%] TaON - Ta	48.0%	68.9%	72.0%
Composition [%] TaON - N	16.0%	20.5%	24.0%
Composition [%] TaON - O	16.0%	23.6%	24.0%
Composition [%] TaN - Ta	64.0%	78.2%	96.0%
Composition [%] TaN - N	16.0%	19.5%	24.0%
Composition [%] TaNRu - Ru	16.0%	16.5%	24.0%
Composition [%] TaNRu - Ta	48.0%	56.0%	72.0%
Composition [%] TaNRu - N	16.0%	20.2%	24.0%
Composition [%] Ru - Ru	80.0%	107.4%	120.0%
Composition [%] Ru2Si3 - Ru	32.0%	39.4%	48.0%
Composition [%] Ru2Si3 - Si	48.0%	65.9%	72.0%
Composition [%] Si - Si	80.0%	107.9%	120.0%
Composition [%] MoSi2 - Si	53.3%	65.8%	80.0%
Composition [%] MoSi2 - Mo	26.7%	32.2%	40.0%
Composition [%] Mo - Mo	80.0%	92.8%	120.0%
Composition [%] MoSi2 - Si	53.3%	79.0%	80.0%
Composition [%] MoSi2 - Mo	26.7%	39.0%	40.0%
Thickness post-etch [nm]	0.000	0.004	3.000
RMS Roughness post-etch [nm]	0.000	0.409	1.000

Table 2. Scatterometry model parameters.

p [nm]	312	469	549	622	820	866	1088	1298
D	0.525	0.350	0.525	0.263	0.337	0.524	0.253	0.335
Thickness [nm] TaON	1.998	1.918	2.097	1.918	1.929	1.919	2.018	2.029
Thickness [nm] TaN	58.56	58.72	59.29	58.54	58.41	58.68	58.36	58.66
RMS Roughness [nm] TaON	0.025	0.021	0.022	0.025	0.022	0.021	0.021	0.022
RMS Roughness [nm] TaN	0.142	0.138	0.116	0.127	0.141	0.132	0.121	0.130
Thickness post-etch [nm]	0.004	0.004	0.004	0.004	0.004	0.004	0.004	0.004
RMS Roughness post-etch [nm]	0.086	0.187	0.041	0.819	0.098	0.728	0.744	0.418

Industry Briefs

Chip Industry Wants $50 Billion to Keep Manufacturing in U.S

Ian King

The U.S. chip industry and the Semiconductor Industry Association said as much as $50 billion in federal incentives will be needed to halt a decades-long trend of manufacturing moving overseas as China spends heavily to become a leading semiconductor producer. The federal government needs to deploy $20 billion to $50 billion to make the U.S. as attractive a location for plants as Taiwan, China, South Korea, Singapore, Israel and parts of Europe.

The lobbying group, which represents companies such as Intel Corp. and Qualcomm Inc., is making the pitch at a time when the China-U.S. trade war and supply-chain disruptions caused by the pandemic have revealed the risks of having such vital components made abroad.

The $400 billion semiconductor industry is led by U.S. companies, but many chipmakers outsource production to factories mostly in Asia. Taiwan Semiconductor Manufacturing Co. dominates that part of the market. The SIA said new U.S. plants built with federal support "would bring state-of-the-art manufacturing technology and sufficient capacity to cover semiconductor demand from the U.S. defense and aerospace industries."

https://www.bloomberg.com/news/articles/2020-09-16/chip-industry-wants-50-billion-to-keep-manufacturing-in-u-s

Global Semiconductor Sales Increase 4.9 Percent Year-to-Year in July

Semiconductor Industry Association

The Semiconductor Industry Association (SIA) announced worldwide sales of semiconductors were $35.2 billion in July 2020, 4.9 percent more than the July 2019 total of $33.5 billion and 2.1 percent greater than the June 2020 total of $34.5 billion. SIA represents 95 percent of the U.S. semiconductor industry by revenue and nearly two-thirds of non-U.S. chip firms.

"The global semiconductor market has remained largely resistant to global macroeconomic headwinds through the first seven months of the year, with sales in July increasing on both a year-to-year and month-to-month basis, but substantial market uncertainty remains for the rest of the year," said John Neuffer, SIA president and CEO. "Sales into the Americas remained strong in July, increasing 26 percent year-to-year, and year-to-year sales were up globally among both memory and non-memory products."

Regionally, sales increased on a year-to-year basis in the Americas (26.3 percent), China (3.5 percent), and Asia Pacific/All Other (1.4 percent), but decreased in Japan (-0.4 percent) and Europe (-14.7 percent). On a month-to-month basis, sales increased across all regions: Asia Pacific/All Other (4.5 percent), Japan (3.4 percent), Europe (3.2 percent), the Americas (0.9 percent), and China (0.5 percent).

https://www.semiconductors.org/global-semiconductor-sales-increase-4-9-percent-year-to-year-in-july/

NVIDIA Acquires Arm to Shake Up Chip Industry

Zeus Kerravala

After months of speculation, GPU king NVIDIA announced Sept. 13 that it is acquiring chip developer/designer Arm from SoftBank for $42 billion, comprising $12 billion in cash, $21.5 billion in stock, a $2 billion payment at signing, $1.5 billion in NVIDIA stock for Arm employees and an additional $5 billion payment based in Arm's performance.

The enormity of this deal highlights just how massive Santa Clara, Calif.-based NVIDIA has become in a relatively short period of time. When SoftBank purchased Arm in 2016, it paid about $32 billion, and NVIDIA's market cap was only about $30 billion. That was a mere four years ago, and NVIDIA is now worth $300 billion, or 10X its valuation back then. The company's growth has been fueled by the demand for its graphics processing units, the main computing unit used to power accelerated computing systems, such as artificial intelligence, ray tracing, self-driving cars, and super computers.

This acquisition also will be another nail in the coffin of rival Intel. For years, NVIDIA was considered a niche gaming company (which it was), while Intel was the king of silicon (which was also true), but over time and through a number of good decisions by NVIDIA and Intel's inability to build a GPU, NVIDIA continued to grow while Intel flat-lined. In July 2020, NVIDIA caught Intel with respect to market cap, and both were worth about $250 billion. Today, Intel has slipped to $209 billion, and NVIDIA is at about $300 billion. The acquisition of Arm will help NVIDIA accelerate the replacement cycle of Intel to Arm by building better-optimized systems in which both CPUs and GPUs are needed.

With the acquisition of Arm, NVIDIA is now able to offer its customers greater flexibility in how things are designed with improved performance. This is a well-timed acquisition by the company, because we are just hitting that inflection point.

https://www.eweek.com/pc-hardware/nvidia-acquires-arm-to-shake-up-chip-industry

Join the premier professional organization for mask makers and mask users!

About the BACUS Group

Founded in 1980 by a group of chrome blank users wanting a single voice to interact with suppliers, BACUS has grown to become the largest and most widely known forum for the exchange of technical information of interest to photomask and reticle makers. BACUS joined SPIE in January of 1991 to expand the exchange of information with mask makers around the world.

The group sponsors an informative monthly meeting and newsletter, BACUS News. The BACUS annual Photomask Technology Symposium covers photomask technology, photomask processes, lithography, materials and resists, phase shift masks, inspection and repair, metrology, and quality and manufacturing management.

Individual Membership Benefits include:

- Subscription to BACUS News (monthly)
- Eligibility to hold office on BACUS Steering Committee

spie.org/bacushome

Corporate Membership Benefits include:

- 3-10 Voting Members in the SPIE General Membership, depending on tier level
- Subscription to BACUS News (monthly)
- One online SPIE Journal Subscription
- Listed as a Corporate Member in the BACUS Monthly Newsletter

spie.org/bacushome

CALENDAR

2021

SPIE Advanced Lithography
21-25 February 2021
San Jose, California, USA
www.spie.org/al

Photomask Japan
26-28 April 2021
Yokohama, Kanagawa, Japan
www.photomask-japan.org

The 36th European Mask and Lithography Conference, EMLC 2021
21-23 June 2021
Leuven, Belgium
www.emlc-conference.com/en

SPIE Photomask Technology + EUV Lithography
September 2021
www.spie.org/conferences-and-exhibitions/photomask-technology--extreme-ultraviolet-lithography

SPIE is the international society for optics and photonics, an educational not-for-profit organization founded in 1955 to advance light-based science and technology. The Society serves more than 255,000 constituents from 183 countries, offering conferences and their published proceedings, continuing education, books, journals, and the SPIE Digital Library in support of interdisciplinary information exchange, professional networking, and patent precedent. In 2019, SPIE provided more than $5 million in community support including scholarships and awards, outreach and advocacy programs, travel grants, public policy, and educational resources. **spie.org**

SPIE.
International Headquarters
P.O. Box 10, Bellingham, WA 98227-0010 USA
Tel: +1 360 676 3290
Fax: +1 360 647 1445
help@spie.org • **spie.org**

Shipping Address
1000 20th St., Bellingham, WA 98225-6705 USA

Managed by SPIE Europe
2 Alexandra Gate, Ffordd Pengam, Cardiff,
CF24 2SA, UK
Tel: +44 29 2089 4747
Fax: +44 29 2089 4750
spieeurope@spieeurope.org • **spieeurope.org**

You are invited to submit events of interest for this calendar. Please send to lindad@spie.org.